Sustainable Energy & Fuels

ROYAL SOCIETY OF CHEMISTRY

PAPER

View Article Online
View Journal | View Issue

Cite this: *Sustainable Energy Fuels*, 2022, **6**, 4884

Pre-lithiated $Li_{4+x}Ti_5O_{12}$ ($0 \leq x \leq 3$) anodes towards building high-performance Li-ion capacitors†

Madhusoodhanan Lathika Divya,[a] Hong-Yan Lü,[b] Yun-Sung Lee *[c] and Vanchiappan Aravindan *[a]

Received 5th August 2022
Accepted 19th September 2022

DOI: 10.1039/d2se01081j

rsc.li/sustainable-energy

Spinel $Li_4Ti_5O_{12}$ is an extensively studied and successfully commercialized battery type electrode for lithium-ion capacitors (LICs), mainly due to its abundance, improved rate capability, and safety guaranteed by the high potential intercalation mechanism. However, still, there is an unanswered question – is prelithiation necessary for LTO-based LIC systems? In this work, we studied the role of prelithiation by assembling different LICs with LTO anodes by varying prelithiation levels ($Li_{4+x}Ti_5O_{12}$, $0 \leq x \leq 3$) with activated carbon (AC) electrodes. The disparities in electrochemical performance of such LICs, energy-power storage capability, and cycling stability are also investigated. The assembled AC/$Li_4Ti_5O_{12}$ cell shows a maximum energy storage capability of 84.59 W h kg^{-1} at a current density of 0.05 A g^{-1}. And, a LIC with an optimum prelithiation level (~30 min (50–55 mA h g^{-1})) and AC/$Li_5Ti_5O_{12}$ configuration exhibits effective utilization of the voltage window. However, the process of prelithiation ensures the cycling stability of such LIC systems.

Introduction

Lithium-ion capacitors (LICs) are hybrid or asymmetric supercapacitors, merging the energy storage mechanisms of lithium-ion batteries (LIBs) and electric double-layer capacitors (EDLCs).[1–4] It is an innovative technology capable of delivering high energy rapidly with long-term cyclability.[5–7] It was first presented by Amatucci *et al.*[8,9] from Telcordia Technologies in 2001. They assembled LICs with nanostructured spinel lithium titanate ($Li_4Ti_5O_{12}$) as the battery type intercalation anode and high surface area activated carbon (AC) as the capacitive type cathode. Thus formed LICs could deliver an energy density of ~20 W h kg^{-1}, nearly 3–5 times that of conventional EDLCs. Since then, this concept of LICs with a battery type anode and an ion adsorption cathode in high-voltage battery electrolytes has continued with further progress accomplished by modifying the electrode–electrolyte system.[10–13] Among different anode materials (carbon materials, transition metal oxides, polyanions, metalloids, carbon composites, *etc.*) used for LIC fabrication, LTO has become the most commonly studied anode material and holds the second largest market share after graphite.[14–16]

LTO is the first studied anode material that gained much attention mainly because of its structural stability during the Li-insertion/extraction reaction, ensuing long-term cyclability in LIC assembly.[17] It is known as a 'zero-strain host' as it shows negligible volume change (<1%) during the lithiation–delithiation process.[18] Moreover, it operates (charge–discharge plateau) at a relatively higher voltage (*ca.* ~1.55 V *vs.* Li^+/Li) within the stability window of conventional carbonate-based electrolytes.[19] Thus, LTO can provide better safety by evading the electrolyte reduction on the electrode surface and avoiding the formation of a solid electrolyte interface (SEI) passivating layer, which might limit the device's power performance. Importantly, the Li-plating issues at high current operation are often faced by carbonaceous electrodes. Spinel LTO ($Li_4Ti_5O_{12}$) has a cubic crystal structure with the $Fd\bar{3}m$ space group and empirical formula $[Li_3]^{8a}[]^{16c}[LiTi_5]^{16d}[O_{12}]^{32e}$, which indicates that Li atoms occupy all the tetrahedral 8a sites and octahedral 16d sites are filled with Li and Ti atoms in a molar ratio of 1 : 5. Moreover, all the 32e sites contain O atoms. The spinel structure offers a 3D network of channels for Li^+ ion diffusion. During lithiation, it takes 3 Li^+ ions per formula and forms a rock salt structure ($Li_7Ti_5O_{12}$) with the empirical formula $[]^{8a}[Li_6]^{16c}[LiTi_5]^{16d}[O_{12}]^{32e}$. The inserted Li atoms occupy octahedral 16c sites and as a result of coulombic interaction between tetrahedral sites (mutual repulsive force between newly inserted and initially present Li^+ ions) cause the migration of Li^+ ions present in the tetrahedral 8a site to octahedral 16c sites in a two-phase separation mechanism with partial reduction of Ti^{4+} to Ti^{3+} ions. Thus, the material exhibits a theoretical discharge capacity of ~175 mA h g^{-1}, which operates between the de-

[a]*Department of Chemistry, Indian Institute of Science Education and Research (IISER), Tirupati 517507, India. E-mail: aravind_van@yahoo.com*

[b]*Department of Chemistry, Northeast Normal University, Changchun, Jilin 130024, China*

[c]*School of Chemical Engineering, Chonnam National University, Gwang-ju, 61186, Republic of Korea. E-mail: leesy@chonnam.ac.kr*

† Electronic supplementary information (ESI) available. See https://doi.org/10.1039/d2se01081j

lithiated spinel state $Li_4Ti_5O_{12}$ and lithiated rock salt state $Li_7Ti_5O_{12}$.[20–23] The equation of the reaction can be represented as:

$$\text{(spinel LTO)}Li_4Ti_5O_{12} + 3Li^+ + 3e^- \leftrightarrow Li_7Ti_5O_{12}\ \text{(rock salt LTO)} \quad (1)$$

However, both spinel and rock salt states of LTO display very similar lattice parameters with ~0.77% lattice shrinkage in the lithiated phase ($Li_7Ti_5O_{12}$; $Fm\bar{3}m$). In addition to cycling stability and safety, factors such as low-cost precursors and easy fabrication methods made LTO an attractive LIC anode. In contrast, limited intrinsic electronic conductivity ($\sim 10^{-13}$ S cm^{-1}) and Li-ion diffusion coefficient ($\sim 10^{-9}$ to 10^{-13} cm^2 s^{-1}) result in poor performance at high current rates.[24–27] But research on different strategies such as nanostructuring, carbon coating, particle morphology optimization, doping, and surface modifications could improve the electrochemical performance of the LTO anode.[28,29]

LICs assembled with LTO anodes and AC cathodes in the presence of an organic electrolyte, lithium hexafluorophosphate in ethylene carbonate and dimethyl carbonate (1M $LiPF_6$ in EC : DMC = 1 : 1) operate by a combination of two different charge storage mechanisms. At the AC cathode, charge storage occurs *via* double layer formation by adsorption of PF_6^- ions across the electrode surface (eqn (2)). On the other hand, at the LTO anode, the charge storage occurs *via* a Li^+ intercalation reaction (eqn (3)).

$$\text{At the cathode: AC} + PF_6^- \leftrightarrow AC^+\ PF_6^-\ \text{(double layer)} \quad (2)$$

$$\text{At the anode: } Li_4Ti_5O_{12} + 3Li^+ + 3e^- \leftrightarrow Li_7Ti_5O_{12} \quad (3)$$

As mentioned, LTO works at 1.55 V *vs.* Li^+/Li, which is much higher than the electrolyte reduction potential (~0.7 V *vs.* Li^+/Li) and ensures a low risk of lithium plating. Hence, such LIC combinations can use lighter and more economical Al current collectors for LTO instead of expensive Cu for graphite-based LICs. However, the lower theoretical capacity (175 mA h g^{-1}) than graphite (372 mA h g^{-1}) and elevated operating potential (1.55 V *vs.* Li^+/Li) than graphite (<0.1 V *vs.* Li^+/Li) are worth mentioning. Among commercial LICs, the LTO and carbonaceous material-based configurations are considered power- and energy type assemblies, respectively. In the case of carbonaceous material-based assembly, it desperately requires a prelithiation process owing to the irreversible decomposition of the electrolyte in the first cycle and wider operating potential.[30] With a hybrid charge storage mechanism in LICs, the optimum design of LICs depends on different design aspects such as the electrode mass ratio, the process of pre-lithiation and electrolyte volume, and the type of electrode–electrolyte separator system.[31,32]

Prelithiation in LICs describes the pre-doping or addition of Li-ions into reversibly transferable (active) sites in the intercalation-based anode and the electrolyte.[6,14,33–35] This is the core of LIC technology and can affect the electrochemical performance of the LIC device in terms of energy storage and cyclability. In contrast, this remains the biggest challenge in terms of procedure complication and cost. In the case of dual carbon LICs, which use carbonaceous materials for the anode and cathode (which do not contain Li^+ ions), prelithiation is essential to endure the continuous Li-insertion/extraction process.[36,37] But in the case of LTO-based LICs, many studies reported that prelithiation is not required.[38,39] Still, some reports specify that it is essential to guarantee increased cell capacity and cycling stability. Rauhala *et al.*[40] compared the performance of AC/LTO-based LICs with and without prelithiation. LICs without prelithiation could provide more specific energy due to minimized active material loading of the LTO anode. They also added that the effective utilization of the AC cathode occurs in the prelithiated LIC where the potential of the LTO anode is stable. Hence, the prelithiated LIC presented increased coulombic efficiency and cycle life. Xu *et al.*[41] stated that the prelithiation of the LTO anode in LIC assembly aids in sidestepping the abrupt potential drop/increase at the LTO anode. They mentioned that it was also helpful to balance the energy loss due to the high initial potential of the AC cathode. They proposed a mathematical model predicting the requirement for an optimal prelithiation level in AC/LTO and pointed out that the prelithiation range was a function of the electrode mass ratio. They conveyed that the prelithiation capacity range (C_{pl}) of $34 \leq C_{pl} \leq 102$ mA h g^{-1} with a mass ratio of 2 and an AC electrode potential of 3.0 V *vs.* Li^+/Li represents the ideal prelithiation range of such a LIC. Recently, Madabattula *et al.*[42,43] studied the need for prelithiation in AC/LTO using a theoretical model and analyzed the role of negative polarization in the AC cathode and the limit of prelithiation to improve the electrochemical performance. Furthermore, the model established a protocol for cycling the LIC without pre-lithiation to avoid the extra cost. In this study, we have experimentally demonstrated for the first time the role of prelithiation and how different levels of prelithiation affect the electrochemical performance of AC/LTO by assembling the LICs and extensively studying the electrochemical aspect. Thus, we believe this work will provide a better understanding to optimize the degree of prelithiation to fabricate a high-performance AC/LTO assembly.

Experimental section

Commercial LTO (Wellcos Corporation, South Korea) and AC (YP 80F Kuraray, Japan; surface area: 2100 m^2 g^{-1}, pore volume: 0.97 ml g^{-1}) were used as anode and cathode active materials for the LIC assembly. The LTO material was characterized by powder X-ray diffraction (XRD, D/teX Ultra 250 diffractometers) utilizing Cu Kα radiation (40 kV, 200 mA, $\lambda = 1.5406$ Å), scanning electron microscopy (SEM S-4700, Hitachi, Japan), energy-dispersive spectroscopy (EDS), and high-resolution transmission electron microscopy (HR-TEM, Tecnai, Philips, Netherlands, 200 keV). The LTO electrodes were prepared by a slurry coating method; the slurry was made by mixing LTO, conductive carbon, and PVdF binder in a ratio of 80 : 10 : 10. After overnight mixing, the slurry was coated on Al-foil using an automatic thick film coater (MSK-AF A-III, MTI Corporation, USA). Furthermore, the foil was dried in a hot air oven for 4 hours and

pressed under a hot roll press (Tester Sangyo, Japan). Electrodes were punched with a 14 mm diameter electrode cutter. AC electrodes were fabricated by mixing AC, conductive carbon (acetylene black), and teflonized acetylene black (TAB-2) binder in a proportion of 80 : 10 : 10 using a mortar and pestle in the presence of ethanol solvent and were pressed on a 16 mm diameter stainless steel mesh current collector (Goodfellow, UK). Both the electrodes were vacuum dried at 75 °C for 4 hours before cell assembly. Using Li metal as the counter/reference electrode, Li/LTO and Li/AC half-cells were assembled. For the LIC assembly, the LTO electrode was first coupled with Li and discharged for different time intervals (30 min, 60 min, and up to complete discharge, ~90 min) to form $Li_5Ti_5O_{12}$, $Li_6Ti_5O_{12}$ & $Li_7Ti_5O_{12}$. These prelithiated electrodes were paired with AC electrodes of balanced mass to create corresponding LICs, such as AC/$Li_5Ti_5O_{12}$, AC/$Li_6Ti_5O_{12}$ & AC/$Li_7Ti_5O_{12}$. In addition, the LTO electrode without prelithiation was also coupled with the AC electrode to form an AC/$Li_4Ti_5O_{12}$ assembly. Both half-cells and LICs (CR 2016-coin cell assembly) were assembled in an Ar-filled glove box using Whatman paper (1825-047, GF/F) as separator and 1M $LiPF_6$ EC : DMC, 1 : 1 v/v (Tomiyama, Japan) as electrolyte.

The electrochemical performance of Li/LTO and Li/AC half-cells and AC/$Li_4Ti_5O_{12}$ AC/$Li_5Ti_5O_{12}$, AC/$Li_6Ti_5O_{12}$ & AC/$Li_7Ti_5O_{12}$ LICs were studied by galvanostatic charge–discharge (GCD), cyclic voltammetry (CV), and electrochemical impedance spectrometry (EIS) techniques using a battery tester (Biologic, France). The potential windows of the half-cells were fixed as 1–2.75 V *vs.* Li^+/Li for the Li/LTO half-cell and 3–4.5 V *vs.* Li^+/Li for the Li/AC half-cell. The assembled LICs were tested within a voltage window of 1–3 V. The EIS Nyquist plot was considered within the frequency range of 10 kHz to 10 mHz at an amplitude of 10 mV. The Ragone plot was designed with energy and power density values of assembled LICs at different current inputs, in which energy and power density values are calculated based on the total mass of the active material in both electrodes.

Results and discussion

The X-ray diffraction (XRD) pattern of the LTO anode material is illustrated in Fig. S1.† The peak positions and peak intensities were in good agreement with JCPDS card number 00-049-0207, which corresponds to a spinel-type cubic structure indexed to the $Fd\bar{3}m$ space group with a lattice parameter of 8.36 Å.[44,45] Scanning electron micrograph (SEM) analysis at different magnifications of LTO powder Fig. 1(a–c) displays micrometer-sized (<15 μm) spherical particles (secondary particles) composed of primary particles of 100–500 nm size.[46] Thus, the spherical-shaped particles are formed by the assembly of primary particles. And it is observed that some of the primary particles are dropped from microspheres. The porous nature of this anode material can ensure decent electrolyte penetration and transport of Li-ions during the charge–discharge process.[47,48] The material's elemental composition was analyzed by energy dispersive spectroscopy (EDS). Fig. 1(d–g) shows the EDS layer image, with elemental mapping corresponding to the presence of C, O, and Ti. The presence of C in the sample indicates carbon contamination which occurs mainly from carbon tape. Except for C, no other impurities were spotted in the LTO material. The transmission electron microscopy (TEM) image of the material is displayed in Fig. 1(h), further explaining the structure of primary particles in the LTO material. The high-resolution transmission electron microscopy (HR-TEM) image in Fig. 1(i) shows a clear lattice fringe with an average

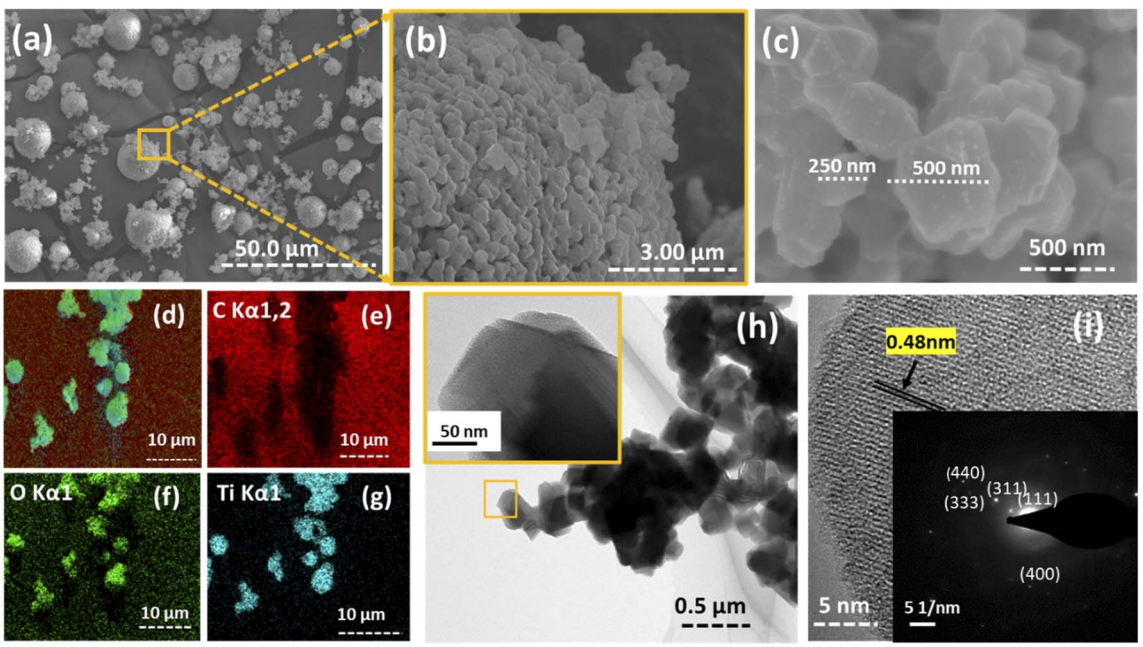

Fig. 1 (a–c) SEM images, (d–g) EDS layered image and corresponding elemental mapping images, (h) TEM image and magnified TEM image in the inset and (i) HRTEM image and the SAED pattern in the inset.

spacing of 0.48 nm corresponding to the (111) plane of the LTO crystal. The selected area diffraction pattern (SAED) in the inset of Fig. 1(i) shows bright diffraction spots, demonstrating the well-defined crystalline nature of LTO.

The LTO and AC-based half-cells (Li/LTO & Li/AC) were fabricated and demonstrated an open circuit voltage (OCV) of ~3.1 & ~3.2 V *vs.* Li/Li^+, respectively. Fig. 2(a) presents the galvanostatic charge–discharge (GCD) profile corresponding to Li-insertion/extraction into LTO and adsorption/desorption of PF_6^- ions on the surface of the AC electrode. The Li/LTO half-cell tested within the potential window of 1–2.75 V *vs.* Li^+/Li exhibited a specific capacity of 177 and 153 mA h g^{-1} at a current density of 100 mA g^{-1} during the insertion and extraction of Li into and out of the crystal lattice. The GCD profile of LTO has a flat and prolonged voltage plateau at around 1.55 V *vs.* Li^+/Li, representing the first-order phase transition (or two-phase reaction) from the spinel phase ($Li_4Ti_5O_{12}$) to the Li-rich rock salt ($Li_7Ti_5O_{12}$) phase, with the reduction of three Ti^{4+} atoms into Ti^{3+} atoms. Many studies have already reported that spinel LTO can lodge up to three lithium ions per formula unit within the considered potential window, with a negligible volume change of 0.2–0.3% corresponding to a lessening lattice constant from 0.836 to 0.835 nm during the process of discharge.[49–52] The capacitive performance of the AC cathode material was also tested within the potential window of 3–4.5 V *vs.* Li^+/Li. The linear GCD profile of the Li/AC half-cell indicates the purely capacitive charge storage mechanism with a discharge capacity of ~53 mA h g^{-1}. As shown in Fig. 2(b), LTO exhibited a discharge capacity of 123 mA h g^{-1} even at a current density of 2 A g^{-1}, which is tailor-made for high-power applications. An increase in current density caused only a slight decrease in the capacity values, which confirms the excellent rate capability of the LTO material. At the end of 500 charge–discharge cycles, the material maintains a discharge capacity of 137 mA h g^{-1}, which is ~76% of the initial capacity value. The initial coulombic efficiency of the Li/LTO half-cell was ~85%, but gradually (after 50 cycles), it increased to >90%. The Li/AC half-cell also showed good cycling stability with a capacity retention of ~90% after 500 charge–discharge cycles (Fig. 2(c)). Moreover, at a high current rate of 1 A g^{-1}, Li/LTO half-cells delivered a discharge capacity of 140 mA h g^{-1} even after 1000 lithiation–delithiation cycles as shown in Fig. S2,† which ensures the robustness of the crystal lattice.

To further estimate the electrochemical properties of the LTO anode material, cyclic voltammetric (CV) and impedance spectroscopy (EIS) studies on Li/LTO half-cells were carried out. Fig. S3† depicts the first four-cycle CV profiles within the potential window of 1–2.75 V *vs.* Li/Li^+ at a scan rate of 0.1 mV s^{-1}. One set of cathodic peaks at 1.66–1.67 V *vs.* Li^+/Li and the corresponding anodic peaks at 1.44–1.49 V *vs.* Li^+/Li represent the reduction (Li-insertion) and oxidation (Li-extraction) processes of the $Ti^{4+/3+}$ couple. Fig. S4(a)† illustrates the CV

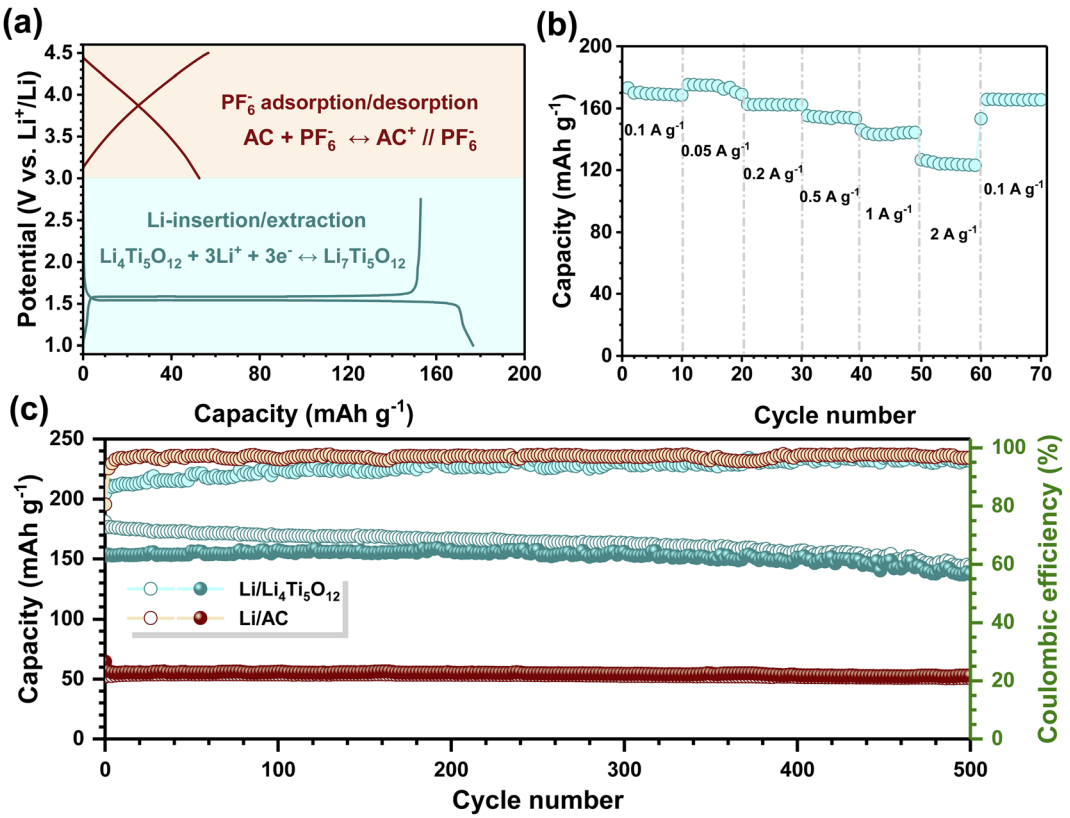

Fig. 2 Electrochemical performance of LTO and AC electrodes in a Li half-cell: (a) typical galvanostatic charge–discharge profile of Li/LTO & Li/AC half-cells at a current density of 100 mA g^{-1}, (b) rate performance of the Li/LTO half-cell at different current rates (0.05–2 A g^{-1}), and (c) cycling stability of Li/LTO & Li/AC half-cells at a current density of 100 mA g^{-1} and their corresponding coulombic efficiencies.

profile at different scan rates (0.1–1 mV s^{-1}) to understand the kinetics of Li-ion migration. The increase in peak potential with increased scan rates indicates a slow rate constant for electron transfer, representing electrode polarization caused by a restricted diffusion process. Fig. S4(b)† presents a plot of anodic and cathodic peak current (i_p) *versus* the square root of the scan rate ($\sqrt{v}$). Linear plots represent the reversible lithiation and de-lithiation of the LTO electrode, and the slope of the plot provides information regarding the stoichiometry of redox reactions. Using the Randles–Sevcik equation, the bulk diffusion coefficient of Li^+ ions (D_{Li^+}) during insertion and extraction was calculated to be 1.5×10^{-10} and 1.42×10^{-10} cm^2 s^{-1}, respectively.[53] We also considered bulk D_{Li^+} for a fresh Li/LTO half-cell from the Warburg tail of the EIS Nyquist plot within the frequency range of 10 kHz to 1 Hz (Fig. S4(c)).† The slope of the graph between the impedance and the inverse square root of angular frequency in the Warburg tail region represents the Warburg coefficient σ (Fig. S4(d)).†[54] The value of σ was obtained as 76.97 Ω s^{-1}, and the corresponding diffusion coefficient was 3.28×10^{-14} cm^2 s^{-1}. Furthermore, the diffusion coefficient of Li^+ ions within the LTO particles was calculated from the low-frequency Warburg diffusion of the LTO anode at different stages of lithiation by considering the concentration of Li-ions in the solid phase of the electrode (Fig. S5).†[55,56] The LTO anode with no prelithiation ($Li_4Ti_5O_{12}$), 30 min prelithiation ($Li_5Ti_5O_{12}$) 60 min prelithiation ($Li_6Ti_5O_{12}$) and complete (90 min) prelithiation ($Li_7Ti_5O_{12}$) represents Li^+ concentrations of 0.0294, 0.0368, 0.044, and 0.0515 mol cm^{-3}, respectively. The corresponding solid-state diffusion coefficients were obtained in the range of 10^{-18} to 10^{-17} cm^2 s^{-1}. The values were slightly varied for different levels of prelithiation, pointing out that there is no linear dependence on the Li concentration because of different energy barriers between the spinel and rock salt phases of LTO.[57] It was reported that the intermediate configurations $Li_5Ti_5O_{12}$ and $Li_6Ti_5O_{12}$, having higher formation energy, exhibit facile Li-ion migration pathways compared with the end phases ($Li_4Ti_5O_{12}$ and $Li_7Ti_5O_{12}$).[50]

To study the electrochemical activity of the prelithiated LTO electrodes ($Li_{4+x}Ti_5O_{12}$, $0 \leq x \leq 3$) in the LIC assembly, these electrodes were coupled with the AC cathode of balanced mass loading. By considering the second discharge capacity of the LTO anode and AC cathode in half-cell assembly, the mass ratio of the cathode to the anode was fixed at 3.3 : 1 for the LIC assembly. The LTO loading for the assembly varies from 1.5 to 2 mg, whereas the AC electrode loading has been accordingly adjusted as per the ratio. Prelithiation of the LTO anode was performed in half-cell assembly by limiting the time of discharge to 30 min (50–55 mA h g^{-1}), 60 min (100–110 mA h g^{-1}), and complete prelithiation (~90 min, 165–180 mA h g^{-1}) to get $Li_5Ti_5O_{12}$, $Li_6Ti_5O_{12}$, and $Li_7Ti_5O_{12}$ forms of LTO, respectively. These prelithiated electrodes were coupled with the AC cathode for the fabrication of LICs, such as AC/

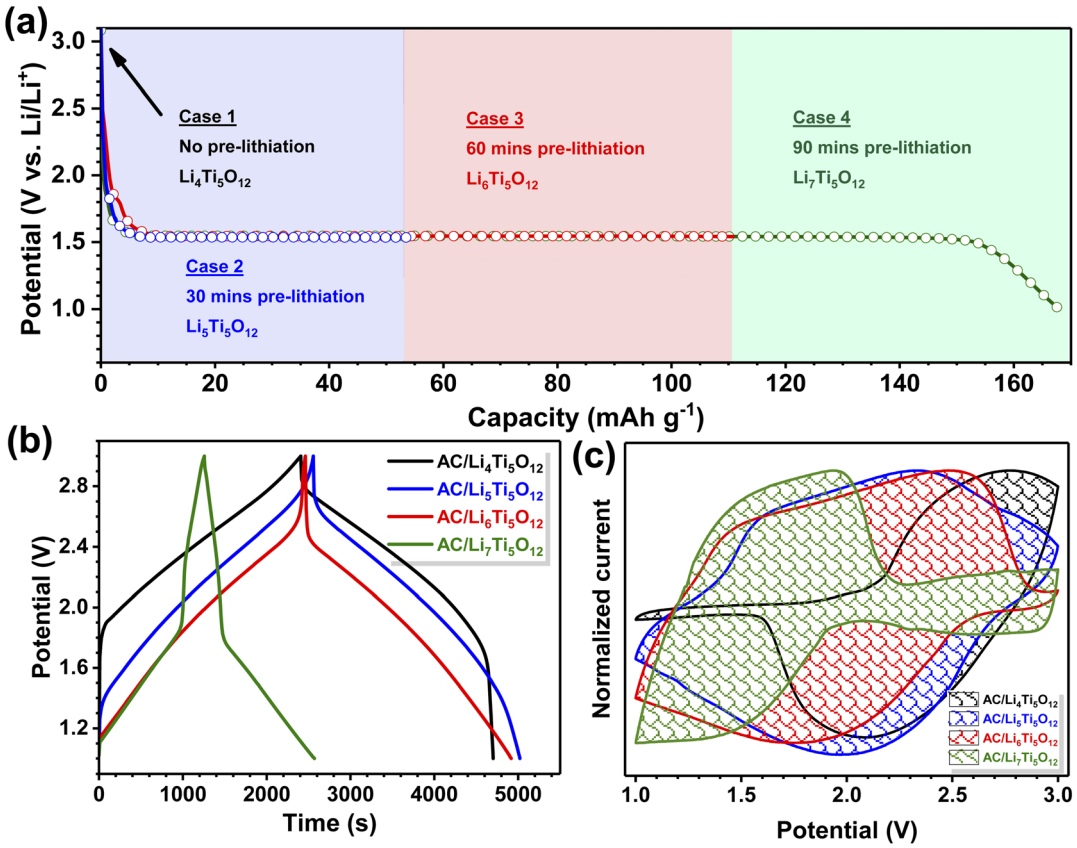

Fig. 3 (a) Discharge profile of the Li/LTO half-cell at different prelithiation levels, (b) comparison graph of the potential *vs.* time plot obtained for all four LIC combinations at a current density of 0.05 A g^{-1}, and (c) comparison graph of CV profiles of all four LICs at a scan rate of 1 mV s^{-1}.

$Li_5Ti_5O_{12}$ (OCV: ~1.52 V), AC/$Li_6Ti_5O_{12}$ (OCV: ~1.52 V), and AC/$Li_7Ti_5O_{12}$ (OCV: ~1.9 V). The LTO electrode without pre-lithiation ($Li_4Ti_5O_{12}$) was also assembled with the AC cathode (AC/$Li_4Ti_5O_{12}$, OCV: ~80–100 mV) for comparison. Fig. 3(a) shows the discharge profile of the LTO anode at different pre-lithiation levels. The flat potential region represents the presence of intermediate crystalline phases $Li_5Ti_5O_{12}$ and $Li_6Ti_5O_{12}$. The GCD and CV analysis of the LICs were executed within the potential window of 1–3 V. Fig. S6(a–d)† depicts the potential *vs.* time graph of the assembled LICs at different current rates (0.05–2 A g^{-1}). The change in the shape of graphs corresponding to LICs of different prelithiation levels indicates the involvement of potential windows in the LIC performance. Fig. 3(b) displays a comparison graph of the potential *vs.* the time plot obtained for all four LIC combinations at a current density of 0.05 A g^{-1}. In the case of AC/$Li_7Ti_5O_{12}$, an abrupt reduction in potential is observed at the upper side of the voltage window, which is completely contradicting the native configuration-based LIC, AC/$Li_4Ti_5O_{12}$. At the same time, almost complete utilization of the voltage window is detected in the case of AC/$Li_5Ti_5O_{12}$, and only a slight drop in potential at the upper side of the voltage window was observed for AC/$Li_6Ti_5O_{12}$. Fig. S6(e–h)† illustrates the CV profile of the assembled LICs at different scan rates (1, 3 & 5 mV s^{-1}). The CV profiles are in good agreement with the corresponding GCD profiles. Fig. 3(c) displays a comparison graph of CV profiles of all four LICs at a scan rate of 1 mV s^{-1}, which shows the complete voltage window utilization in the case of the AC/$Li_5Ti_5O_{12}$ LIC in comparison with other LIC combinations. Apparently, there is a 180° shift in the faradaic region of the voltage window of LICs assembled with $Li_4Ti_5O_{12}$ and $Li_7Ti_5O_{12}$. For the AC/$Li_4Ti_5O_{12}$ LIC, the CV profile shows the position of redox peaks at the higher end of the voltage window; however, for the AC/$Li_7Ti_5O_{12}$ LIC, it is shifted to the lower end of the voltage window. This shift is also clear from the GCD profiles of the LICs. The presence of Li-rich and deficient phases and associated OCVs are the main reasons for this shift. Generally, the AC/$Li_4Ti_5O_{12}$-based LICs with an OCV below ~300 mV exhibited underutilization of the lower side of the voltage window; however, AC/$Li_7Ti_5O_{12}$ with an OCV above 1.5 V showed effective utilization of the downside of the voltage window. The electrolyte is the only source for the Li-ions during the charge–discharge process of AC/$Li_4Ti_5O_{12}$-based LICs. However, in the case of pre-lithiated anodes, $Li_{4+x}Ti_5O_{12}$, the plentiful amount of Li-ions in the host lattice, besides the electrolytes, leads to an OCV of >1.5 V. As a result, a notable shift in the faradaic region is observed. In other words, the state of charge is mainly responsible for this; for instance, AC/$Li_4Ti_5O_{12}$-based LICs are first charged during this testing, whereas AC/$Li_{4+x}Ti_5O_{12}$-based LICs first undergo the discharge process due to the availability of the free Li-ions in the host lattice. Thus, in the CV profile, the active region of the voltage window of both the LICs displayed a difference of 180° between them. Since LTO obeys the "shrinking-core" model for the two-phase reaction, the presence of such phases is easily identified by conducting EIS studies.[58] The signature of the two-phase reaction is the very sharp redox

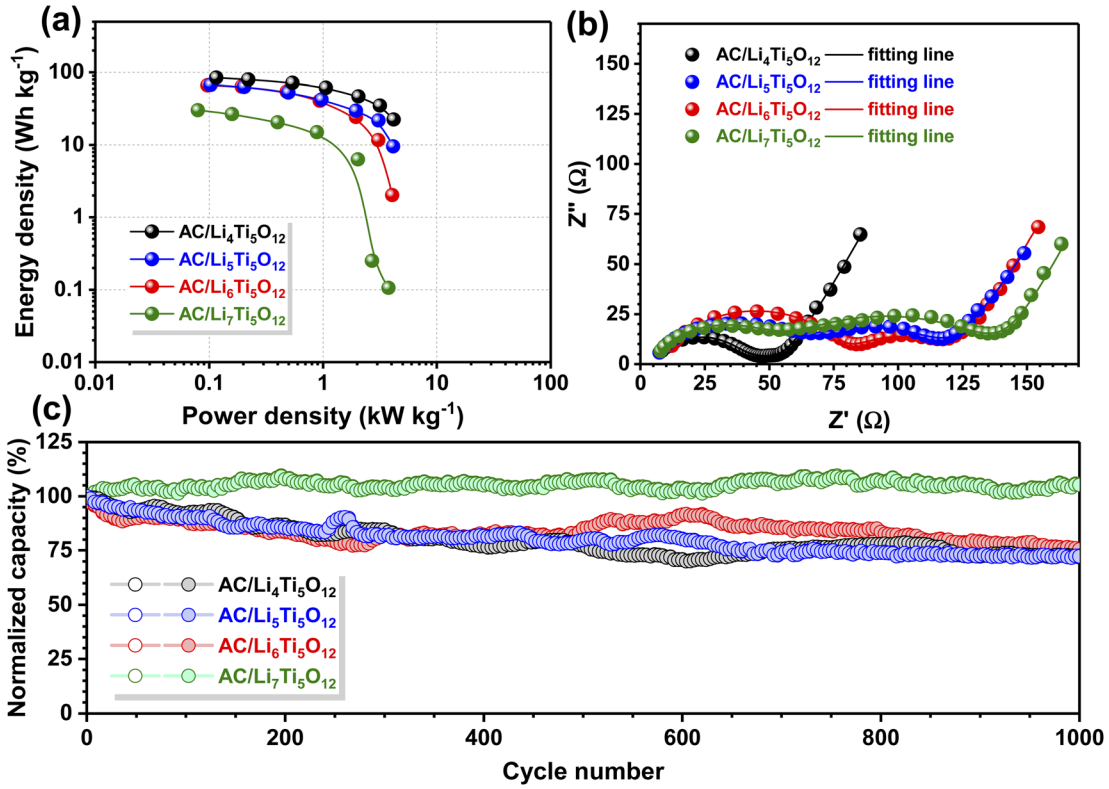

Fig. 4 (a) Ragone plot of the assembled LICs at different current rates, (b) EIS Nyquist plot recorded for the assembled LIC configurations within the frequency limit of 10 kHz to 10 mHz, and (c) long-term cycling performance of the assembled LICs at a current density of 1 A g^{-1}.

peak positions observed during the electrochemical cycling. In addition to LTO, $LiFePO_4$-based LIC systems may also exhibit this faradaic shift in the effective voltage region due to the two-phase formation nature and flat OCV.

Fig. 4(a) illustrates the Ragone plot representing the energy and power density of assembled LICs at different current input values. The AC/$Li_4Ti_5O_{12}$ cell demonstrated better performance than the other three LIC combinations with a prelithiated LTO anode. The AC/$Li_4Ti_5O_{12}$ assembly could deliver a maximum energy density of 84.59 W h kg^{-1} with a power density of 115 W kg^{-1} (at a current density of 0.05 A g^{-1}). However, AC/$Li_5Ti_5O_{12}$ and AC/$Li_6Ti_5O_{12}$-based LICs exhibited almost similar performance with maximum energy density values of ~67 W h kg^{-1}. In contrast, the fully lithiated AC/$Li_7Ti_5O_{12}$ configuration demonstrated poor energy storage capability, mainly at high power density values. Fig. 4(b) shows the EIS Nyquist plot recorded for the assembled LIC configurations within the frequency limit of 10 kHz to 10 mHz. The Nyquist plot of AC/$Li_4Ti_5O_{12}$ LIC consists of a semi-circle in the high-frequency region representing charge transfer resistance (R_{ct}) and a low-frequency Warburg tail corresponding to diffusion of Li-ions in the electrodes. The intercept on the x-axis in the high-frequency region indicates the value of electrolyte resistance (R_s). As LTO is a two-phase material and avoids electrolyte reduction and hence SEI layer formation, the appearance of two semi-circles for the LICs with prelithiated LTO anodes can be associated with the development of two different phases, such as Li-deficient ($Li_4Ti_5O_{12}$) and Li-rich ($Li_7Ti_5O_{12}$). It is understood from the Nyquist plot that prelithiation could effectively separate these two phases. Apparently, similar to olivine $LiFePO_4$, the LTO phase also involves the Li-storage process *via* the "shrinking-core" model, in which Li-rich and deficient phases are clearly evident.[23] The change in semi-circles' size indicates the variation in concentrations of both phases. EIS is one of the powerful tools to segregate such phases; for example, Sabet and Sauer[59] thoroughly analyzed the Li-ion concentration in $LiNi_{0.4}Mn_{0.4}Co_{0.2}O_2$/graphite cells with state-of-charge by conducting *in situ* EIS studies with variation in the size of the semi-circle which is similar to that in our pre-lithiated LTO anodes. For AC/$Li_7Ti_5O_{12}$, it is very clear that the size of the second semi-circle corresponding to the Li-rich ($Li_7Ti_5O_{12}$) phase is at a higher concentration. It was also sensed that the overall resistance of the LIC system is increasing with the degree of prelithiation. Fig. S7† gives the equivalent circuit model to fit the EIS data of assembled LICs. Fig. 4(c) illustrates the long-term cycling performance of the assembled LICs at a current density of 1 A g^{-1}. AC/$Li_7Ti_5O_{12}$ cells could work for over 1000 cycles without a noticeable decrease in capacity. In contrast, other LIC configurations could maintain >70% of the initial capacity after 1000 charge–discharge cycles. It is also observed that LICs with partially prelithiated LTO anodes could attain marginally better capacity retention than the one without prelithiation (AC/$Li_4Ti_5O_{12}$). This capacity fade in the AC/$Li_4Ti_5O_{12}$-based LIC system may be due to the loss of the active material in the lithiated/de-lithiated state or due to the loss of Li inventory (LLI).[42] Particle cracking, development of resistive layers on the active sites during side reactions between the electrode and electrolyte, and also loss of electrical connectivity between particles may result in a dip in the active material content. Consumption of Li during decomposition and other parasitic reactions may result in LLI. However, the pre-lithiation strategy can effectively improve cycling stability by mitigating the effect of Li loss due to side reactions. Moreover, the LTO anode without prelithiation in the AC/LTO LIC assembly is subjected to a significant potential variation during discharge of the cell, and that causes underutilization of the AC cathode, which has a negative impact on the LIC performance. Optimum pre-lithiation in the LTO anode can make use of the extra Li content due to prelithiation and can also exhibit effective involvement of the AC cathode and capacitive retention for LIC assembly. However, the completely prelithiated LTO anode exhibited poor performance due to increased resistance and limited voltage window utilization. So optimal prelithiation (~50–100 mA h g^{-1}) can be considered as an effective method to compensate for Li loss, to prevent sudden voltage drift (drop or increase) during charging and discharging of the LTO anode and also to ensure effective utilization of the AC cathode in AC/LTO based LIC systems. Further studies are in progress to probe more insights into the $Li_{4+x}Ti_5O_{12}$ anode towards the shift of the faradaic region upon pre-lithiation irrespective of the concentrations.

Conclusion

In summary, we studied the need for pre-lithiation in the LTO anode for LIC assembly with a mass ratio corresponding to a balanced capacity at both electrodes. The GCD and CV analyses showed unusual electrochemical activity of pre-lithiated $Li_{4+x}Ti_5O_{12}$, $0 \leq x \leq 3$ anodes in the LIC assembly. There is a 180° faradaic shift in the CV profile of the assembled LICs, with $Li_4Ti_5O_{12}$ and $Li_7Ti_5O_{12}$ anodes. Active utilization of the voltage window was detected for the LICs with intermediate $Li_5Ti_5O_{12}$ & $Li_6Ti_5O_{12}$ phase-based configurations. However, prelithiation could effectively reduce the capacity fade in the LIC assembly. This study concludes that the step of pre-lithiation is not crucial for the assembly of AC/LTO LICs while considering the energy-power storage capability. But, an optimal prelithiation of the LTO anode, $Li_5Ti_5O_{12}$, could avoid a sudden drop in potential at the lower side of the voltage window. Moreover, prelithiation could guarantee the cycling stability of the LIC by providing lithium inventory.

Conflicts of interest

The authors declare that they have no known competing financial interests.

Acknowledgements

MLD wishes to thank the funding through Women Scientist Scheme – B (DST/WOSB/2018/2039) from the KIRAN division of the DST, Govt. of India. YSL acknowledges the financial support from the National Research Foundation of Korea (NRF) grant funded by the Korean government (Ministry of Science,

ICT&Future Planning) (No. 2019R1-A2C1007620). VA acknowledges financial support from the Science and Engineering Research Board, a statutory body of the DST, Govt. of India, through the Swarnajayanti Fellowship (SB/SJF/2020-21/12).

References

1 J. Ding, W. Hu, E. Paek and D. Mitlin, *Chem. Rev.*, 2018, **118**, 6457–6498.
2 J. J. Lamb and O. S. Burheim, *Energies*, 2021, **14**, 979.
3 M. L. Divya, S. Natarajan, Y.-S. Lee and V. Aravindan, *ChemSusChem*, 2019, **12**, 4353–4382.
4 V. Aravindan and Y.-S. Lee, *J. Phys. Chem. Lett.*, 2018, **9**, 3946–3958.
5 A. Jagadale, X. Zhou, R. Xiong, D. P. Dubal, J. Xu and S. Yang, *Energy Storage Mater.*, 2019, **19**, 314–329.
6 L. Jin, C. Shen, A. Shellikeri, Q. Wu, J. Zheng, P. Andrei, J.-G. Zhang and J. P. Zheng, *Energy Environ. Sci.*, 2020, **13**, 2341–2362.
7 M. L. Divya and V. Aravindan, *Chem.–Asian J.*, 2019, **14**, 4665–4672.
8 G. G. Amatucci, F. Badway, A. Du Pasquier and T. Zheng, *J. Electrochem. Soc.*, 2001, **148**, A930.
9 A. Du Pasquier, I. Plitz, S. Menocal and G. Amatucci, *J. Power Sources*, 2003, **115**, 171–178.
10 L. Li, D. Zhang, J. Deng, Y. Gou, J. Fang, H. Cui, C. Zhang and M. Cao, *Sustainable Energy Fuels*, 2021, **5**, 3278–3291.
11 S. Yi, L. Wang, X. Zhang, C. Li, W. Liu, K. Wang, X. Sun, Y. Xu, Z. Yang, Y. Cao, J. Sun and Y. Ma, *Sci. Bull.*, 2021, **66**, 914–924.
12 R. Kang, W.-Q. Zhu, S. Li, B.-B. Zou, L.-L. Wang, G.-C. Li, X.-H. Liu, D. H. L. Ng, J.-X. Qiu, Y. Zhao, F. Qiao and J.-B. Lian, *Rare Met.*, 2021, **40**, 2424–2431.
13 Y. An, T. Liu, C. Li, X. Zhang, T. Hu, X. Sun, K. Wang, C. Wang and Y. Ma, *J. Mater. Chem. A*, 2021, **9**, 15654–15664.
14 J. Zheng, G. Xing, L. Zhang, Y. Lu, L. Jin and J. P. Zheng, *Batteries Supercaps*, 2021, **4**, 897–908.
15 S. Natarajan, Y. S. Lee and V. Aravindan, *Chem.–Asian J.*, 2019, **14**, 936–951.
16 V. Aravindan, J. Gnanaraj, Y.-S. Lee and S. Madhavi, *Chem. Rev.*, 2014, **114**, 11619–11635.
17 S. Chauque, F. Y. Oliva, A. Visintin, D. Barraco, E. P. M. Leiva and O. R. Cámara, *J. Electroanal. Chem.*, 2017, **799**, 142–155.
18 C. Han, H. Li, R. Shi, L. Xu, J. Li, F. Kang and B. Li, *Energy Environ. Mater.*, 2018, **1**, 75–87.
19 T. Akintola, A. Shellikeri, T. Akintola and J. P. Zheng, *Batteries*, 2021, **7**, 33.
20 M. G. Verde, L. Baggetto, N. Balke, G. M. Veith, J. K. Seo, Z. Wang and Y. S. Meng, *ACS Nano*, 2016, **10**, 4312–4321.
21 C. Han, Y.-B. He, M. Liu, B. Li, Q.-H. Yang, C.-P. Wong and F. Kang, *J. Mater. Chem. A*, 2017, **5**, 6368–6381.
22 Y. Chen, H. Pan, C. Lin, J. Li, R. Cai, S. J. Haigh, G. Zhao, J. Zhang, Y. Lin, O. V. Kolosov and Z. Huang, *Adv. Funct. Mater.*, 2021, **31**, 2105354.
23 B. Zhao, R. Ran, M. Liu and Z. Shao, *Mater. Sci. Eng., R*, 2015, **98**, 1–71.
24 Y. Liu, W. Wang, J. Chen, X. Li, Q. Cheng and G. Wang, *J. Energy Chem.*, 2020, **50**, 344–350.
25 X. Liang, R. Qi, M. Zhao, Z. Zhang, M. Liu, X. Pu, Z. L. Wang and X. Lu, *Energy Storage Mater.*, 2020, **24**, 297–303.
26 A. Richa, H. Yong, S. Yin, C. Chunhui and W. Chunlei, Hybridization of lithium-ion batteries and electrochemical capacitors: fabrication and challenges, *Proc. SPIE*, 2015, **9493**, 94930B.
27 P. Han, G. Xu, X. Han, J. Zhao, X. Zhou and G. Cui, *Adv. Energy Mater.*, 2018, **8**, 1801243.
28 J. Ni, L. Yang, H. Wang and L. Gao, *J. Solid State Electrochem.*, 2012, **16**, 2791–2796.
29 K. Naoi, S. Ishimoto, J.-i. Miyamoto and W. Naoi, *Energy Environ. Sci.*, 2012, **5**, 9363–9373.
30 X. Yao, S. Xie, C. Chen, Q. Wang, J. Sun, Y. Li and S. Lu, *Electrochim. Acta*, 2005, **50**, 4076–4081.
31 S. Dsoke, B. Fuchs, E. Gucciardi and M. Wohlfahrt-Mehrens, *J. Power Sources*, 2015, **282**, 385–393.
32 A. Jain, V. Aravindan, S. Jayaraman, P. S. Kumar, R. Balasubramanian, S. Ramakrishna, S. Madhavi and M. P. Srinivasan, *Sci. Rep.*, 2013, **3**, 3002.
33 F. Holtstiege, P. Bärmann, R. Nölle, M. Winter and T. Placke, *Batteries*, 2018, **4**, 4.
34 C. Sun, X. Zhang, C. Li, K. Wang, X. Sun and Y. Ma, *Energy Storage Mater.*, 2020, **32**, 497–516.
35 X. Sun, P. Wang, Y. An, X. Zhang, S. Zheng, K. Wang and Y. Ma, *J. Electrochem. Soc.*, 2021, **168**, 110540.
36 S. S. Zhang, *Batteries Supercaps*, 2020, **3**, 1137–1146.
37 M. L. Divya, S. Natarajan, Y.-S. Lee and V. Aravindan, *J. Mater. Chem. A*, 2020, **8**, 4950–4959.
38 B. Li, H. Zhang, D. Wang, H. Lv and C. Zhang, *RSC Adv.*, 2017, **7**, 37923–37928.
39 B. Babu, P. G. Lashmi and M. M. Shaijumon, *Electrochim. Acta*, 2016, **211**, 289–296.
40 T. Rauhala, J. Leis, T. Kallio and K. Vuorilehto, *J. Power Sources*, 2016, **331**, 156–166.
41 N. Xu, X. Sun, F. Zhao, x. Jin, X. Zhang, K. Wang, K. Huang and Y. Ma, *Electrochim. Acta*, 2017, **236**, 443–450.
42 G. Madabattula, B. Wu, M. Marinescu and G. Offer, *J. Electrochem. Soc.*, 2020, **167**, 043503.
43 G. Madabattula, B. Wu, M. Marinescu and G. Offer, *J. Electrochem. Soc.*, 2019, **167**, 013527.
44 L. Tang, Y.-B. He, C. Wang, S. Wang, M. Wagemaker, B. Li, Q.-H. Yang and F. Kang, *Adv. Sci.*, 2017, **4**, 1600311.
45 M. R. Sovizi and S. M. Pourali, *J. Electron. Mater.*, 2018, **47**, 6525–6531.
46 K. Qian, L. Tang, M. Wagemaker, Y.-B. He, D. Liu, H. Li, R. Shi, B. Li and F. Kang, *Adv. Sci.*, 2017, **4**, 1700205.
47 S.-C. Hsu, T.-T. Huang, Y.-J. Wu, C.-Z. Lu, H. C. Weng, J.-H. Huang, C.-W. Chang-Jian and T.-Y. Liu, *Polymers*, 2021, **13**, 1672.
48 Y. Kim, H. Seo, E. Kim, J. Kim and I. Seo, *Nanomaterials*, 2020, **10**, 1705.
49 X. Sun, P. Radovanovic and B. Cui, *New J. Chem.*, 2014, **39**, 38–63.
50 W. Zhang, D.-H. Seo, T. Chen, L. Wu, M. Topsakal, Y. Zhu, D. Lu, G. Ceder and F. Wang, *Science*, 2020, **367**, 1030–1034.

51 M. M. Thackeray and K. Amine, *Nat. Energy*, 2021, **6**, 683–683.
52 T. A. Assefa, A. F. Suzana, L. Wu, R. J. Koch, L. Li, W. Cha, R. J. Harder, E. S. Bozin, F. Wang and I. K. Robinson, *ACS Appl. Energy Mater.*, 2021, **4**, 111–118.
53 Y. Wang, Y.-x. Zhang, W.-J. Yang, S. Jiang, X.-w. Hou, R. Guo, W. Liu, P. Huang, J. Lu, H.-t. Gu and J.-y. Xie, *J. Electrochem. Soc.*, 2019, **166**, A5014–A5018.
54 U. V. Kawade, M. S. Jayswal, A. A. Ambalkar, S. R. Kadam, R. P. Panmand, J. D. Ambekar, M. V. Kulkarni and B. B. Kale, *RSC Adv.*, 2018, **8**, 38391–38399.
55 M. Ma, A. N. Mansour, J. K. Ko, G. H. Waller and C. E. Hendricks, *J. Electrochem. Soc.*, 2020, **167**, 110549.
56 M. Krajewski, B. Hamankiewicz, M. Michalska, M. Andrzejczuk, L. Lipinska and A. Czerwinski, *RSC Adv.*, 2017, **7**, 52151–52164.
57 B. Ziebarth, M. Klinsmann, T. Eckl and C. Elsässer, *Phys. Rev. B: Condens. Matter Mater. Phys.*, 2014, **89**, 174301.
58 M. Gaberšček, *Nat. Commun.*, 2021, **12**, 6513.
59 P. Shafiei Sabet and D. U. Sauer, *J. Power Sources*, 2019, **425**, 121–129.

